coatings

MDPI

Article

Rational Construction of $LaFeO_3$ Perovskite Nanoparticle-Modified TiO_2 Nanotube Arrays for Visible-Light Driven Photocatalytic Activity

Jiangdong Yu [1,2], Siwan Xiang [1], Mingzheng Ge [3], Zeyang Zhang [1], Jianying Huang [4], Yuxin Tang [5,6], Lan Sun [1,2,*], Changjian Lin [1] and Yuekun Lai [4,*]

1 State Key Laboratory of Physical Chemistry of Solid Surface, Department of Chemistry, College of Chemistry and Chemical Engineering, Xiamen University, Xiamen 361005, China; yujiangdong@stu.xmu.edu.cn (J.Y.); xiangsiwan@stu.xmu.edu.cn (S.X.); 20520171151374@stu.xmu.edu.cn (Z.Z.); cjlin@xmu.edu.cn (C.L.)
2 Shenzhen Research Institute of Xiamen University, Shenzhen 518000, China
3 College of Textile and Clothing Engineering, Soochow University, Suzhou 215006, China; mzge1990@ntu.edu.cn
4 College of Chemical Engineering, Fuzhou University, Fuzhou 350116, China; jyhuang@fzu.edu.cn
5 School of Materials Science and Engineering, Nanyang Technological University, 50 Nanyang Avenue, Singapore 639798, Singapore; yxtang@ntu.edu.sg
6 Institute of Applied Physics and Materials Engineering, University of Macau, Macao, China
* Correspondence: sunlan@xmu.edu.cn (L.S.); yklai@fzu.edu.cn (Y.L.)

Received: 27 August 2018; Accepted: 20 October 2018; Published: 23 October 2018

Abstract: $LaFeO_3$ nanoparticle-modified TiO_2 nanotube arrays were fabricated through facile hydrothermal growth. The absorption edge of $LaFeO_3$ nanoparticle-modified TiO_2 nanotube arrays displaying a red shift to ~540 nm was indicated by the results of diffuse reflectance spectroscopy (DRS) when compared to TiO_2 nanotube arrays, which means that the sample of $LaFeO_3$ nanoparticle-modified TiO_2 nanotube arrays had enhanced visible light response. Photoluminescence (PL) spectra showed that the $LaFeO_3$ nanoparticle-modified TiO_2 nanotube arrays efficiently separated the photoinduced electron–hole pairs and effectively prolonged the endurance of photogenerated carriers. The results of methylene blue (MB) degeneration under simulated visible light illumination showed that the photocatalytic activity of $LaFeO_3$ nanoparticle-modified TiO_2 nanotube arrays is obviously increased. $LaFeO_3$ nanoparticle-modified TiO_2 nanotube arrays with 12 h hydrothermal reaction time showed the highest degradation rate with a 2-fold enhancement compared with that of pristine TiO_2 nanotube arrays.

Keywords: TiO_2 nanotube; $LaFeO_3$; perovskite; heterojunction; visible light driven; photocatalysis

1. Introduction

In recent decades, the application of TiO_2 nanomaterials in photocatalytic purification of organic contaminants has been widely used owing to its non-toxicity, superior redox potentials, long term thermodynamic stability, chemical inertness, and high photocatalytic activity [1–9]. The main drawbacks of TiO_2 are its wide band-gap (3.0–3.2 eV) which limits the light absorption to UV-light (ca. 4%), and fast recombination of photoinduced electron–hole pairs [10]. In order to improve the catalytic efficiency, it is crucial for a catalyst to be sensitive to solar light irradiation. In addition, an efficient separation of photogenerated electrons and holes could better trigger chemical reactions either by electrons or holes [11]. Nowadays, doping is viewed as an advanced strategy of narrowing the bandgap and improving light absorption of a catalyst by forming more delocalized intra-band states, including metal/nonmetal ion doping and co-doping [12–14]. However, this doping method has little

effect of inhibiting the photoinduced electron–hole pairs from recombination [15]. Another approach is to develop new heterojunctions using visible light to initiate photocatalytic reactions. As such, one technique to enhance the photocatalytic activity, coupled catalysts, bears the merits of accelerating the partition of electron–hole pairs, and effectively extends the UV light utilization to the visible light absorption region.

Recently, a considerable amount of attention has been paid to perovskite-type ABO_3 transition-metal oxides in the photocatalytic field thanks to its small band gap (2.0–2.5 eV) and high chemical stability [16–18]. Among the well-known ABO_3 perovskites, $LaFeO_3$ (LFO) has been well-known as a visible-light-sensitive photocatalyst due to its suitable bandgap (~2.1 eV). Therefore, the construction of heterojunction composites based on TiO_2 modified with LFO has great potential to improve its photocatalytic performance, as this hybrid design enjoys a favorable alignment between band offset and energy levels [19]. In such an architecture, a narrow bandgap LFO could be easily activated by visible light. In addition, coupling with wide bandgap oxide TiO_2, heterostructures make the division of the desired device's functions (e.g., light absorption and long-range carrier transfer) between coupled materials more feasible [20].

In previous works, highly ordered TiO_2 nanotube array (TNT) film has been explored as an excellent substrate for photoanode due to its fast electron transmission, preferable mechanical properties, and large specific surface area [21–23]. On the other hand, the merit of using smaller band gap LFO nanoparticles is their activation by visible light. However, the synthesis of ABO_3 perovskites have generally been accomplished by solid-state reaction [24], sol-gel [25], and combustion methods [26] which require high temperature (>900 °C) that would destroy the nanotube structure of TNTs [27] and result in severe agglomeration of the micrometer-sized particles. To solve this issue, we have assessed wet chemical methods. By comparing diverse wet chemical routines, a hydrothermal method is one of the best synthetic methods for fabricate nano-materials. The main advantages of this strategy are its simplicity, controllable size, effective cost, and low temperature growth [28]. Therefore, it is a facile and appealing approach for the synthesis of LFO nanoparticle-modified TNTs (LFO/TNTs).

In this work, a LFO/TNTs heterojunction nanocomposite has been fabricated by an electrochemical anodization technique and subsequently by a hydrothermal approach process using a lanthanum citrate and ion citrate coordination complex. The as-prepared materials have been thoroughly characterized by scanning electron microscope (SEM), X-ray diffraction (XRD), X-ray photoelectron spectroscopy (XPS), UV-Vis diffuse reflectance spectroscopy (DRS), and photoluminescence (PL) spectra. The results of the photocatalytic experiment show that LFO/TNTs have outstanding photocatalytic activity of photodegradation of methylene blue (MB) compared to that of pure TNTs in the visible-light range.

2. Materials and Methods

The vertically-aligned and highly ordered TNTs were synthesized using a previously described method. Before anodization, 1 × 1.5 cm^2 Ti foil (purity > 99%, thickness of 0.1 mm) was soaked in a bath of acetone, alcohol, and distilled water for 15 min under ultrasonic conditions. The processed Ti foil was then dipped in the 0.5 wt % HF aqueous solution with applied voltage. The set-up for anodization was a simple two-electrode cell set at 20 V for 30 min at room temperature, in which Ti foil and Pt foil were applied as the working electrode and counter electrode, respectively. Subsequently, the sample was taken out of the HF solution and rinsed with deionized water immediately to get rid of the residual HF. Afterwards, the achieved amorphous TNTs were annealed in a muffle oven with a heating rate of 5 °C min^{-1} and kept at 450 °C for 2 h, and then cooled to room temperature naturally.

The $LaFeO_3$ nanoparticle-modified TNTs were synthesized by the hydrothermal reaction carried out in a stainless steel autoclave. In a typical experiment, initially, based on the stoichiometric composition of the reactants, both lanthanum nitrate ($La(NO_3)_3 \cdot 6H_2O$) and ferric nitrate ($Fe(NO_3)_3 \cdot 9H_2O$) were dissolved in deionized water to achieve a mixed solution of 5 mM. Next, citric acid with mole ratio of 1:1:2 was added to the mixed solution as a stabilizer. Subsequently, the mixture was transferred into an autoclave with an

as-prepared TNTs sample at the bottom, and kept at 160 °C for 8 h, 10 h, 12 h, and 14 h. After cooling, the sample was washed several times with deionized water, followed by annealing at 550 °C for 2 h to obtain LFO/TNTs. All chemicals and reactants used in this work were analytical reagents (AR).

The structure and morphology of the as-prepared samples were characterized by using a field emission scanning electron microscope (FESEM, Hitachi S4800, Hitachi, Tokyo, Japan). Crystal information was identified by X-ray diffraction (XRD, Phillips, Panalytical X'pert, PANalytical, B.V., the Netherlands, Cu Kα radiation (λ = 1.5417 Å)). The elemental composition was measured by X-ray photoelectron spectroscopy (XPS, VG, Physical Electrons Quantum 2000 Scanning Esca Microprobe, Al Kα radiation, Physical Electronics, Chanhassen, MN, USA). UV-visible diffuse reflectance spectra (DRS) of the as-prepared samples were analyzed using a UV-Vis-NIR spectrophotometer (Varian Cary 5000, Varian Medical Systems, Palo Alto, CA, USA). Photoluminescence (PL) spectra were recorded by a Hitachi F-7000 spectrophotometer (Hitachi F7000, Hitachi, Tokyo, Japan). All degeneration MB dye was performed under aerobic conditions in a home-made quartz glass reactor without bias voltage applied, whose temperature can be controlled through the equipped water jacket. During the degradation process, 3 mL of solution was periodically extracted from the reactor and detected by a UV-Vis spectrophotometer (Unico UV-2102 PC, Unico, Shanghai, China).

3. Results and Discussion

As shown in Figure 1a,b, the top and side view SEM images of pure TNTs demonstrate vertically aligned and highly ordered TiO_2 nanotubes with tube length of about 350 nm and an average tube diameter of around 100 nm. It can be seen from Figure 1b that the inner wall of the TNTs is clean and smooth and some thin, broken TiO_2 films cling to the top surface of the nanotubes. Figure 1c–f shows the SEM images of LFO/TNTs prepared with different hydrothermal reaction times. After loading LFO nanoparticles onto the TNTs, the interstitial space around the surface edge of the walls and between nanotubes is occupied by additional nanoparticles ranging in size from 30 to 50 nm. The LFO nanoparticles manifests as rounded corners with rectangular or rough ellipsoid shape, with a drastically increasing amount almost totally covering all the openings of the nanotubes following hydrothermal reaction of up to 14 h. Interestingly, when the hydrothermal reaction time is 12 h (LFO/TNTs-12h, Figure 1e), clusters of LFO nanoparticles are formed circling around the openings of the nanotubes, with some of them having permeated into the tubes (inset of Figure 1e).

Figure 2 shows the XRD patterns of TNTs, LFO/TNTs, and LFO powder. For TNTs, the diffraction peak at 2θ = 25.3 was attributed to the anatase TiO_2 (101) crystal planes. It is worth noting that the signal intensity of anatase TiO_2 is relatively weak, though the abundance of TiO_2 nanotubes fully covers the surface of Ti foil substrate. Yet, when it comes to LFO, no signal could be detected from LFO/TNTs at all. Nevertheless, the crystal structure and phase composition of LFO were characterized by the powder XRD patterns of the as-prepared sample collected from of the superfluous sediment in the Teflon-liner and annealed at 550 °C However, peaks corresponding to La_2O_3, Fe_2O_3, or other crystalline contaminations were not distinguished, indicating that the product is single phase LFO. We believe the subtlety of the signal of LFO in LFO/TNTs is due to the extremely high signal intensity of Ti foil substrate.

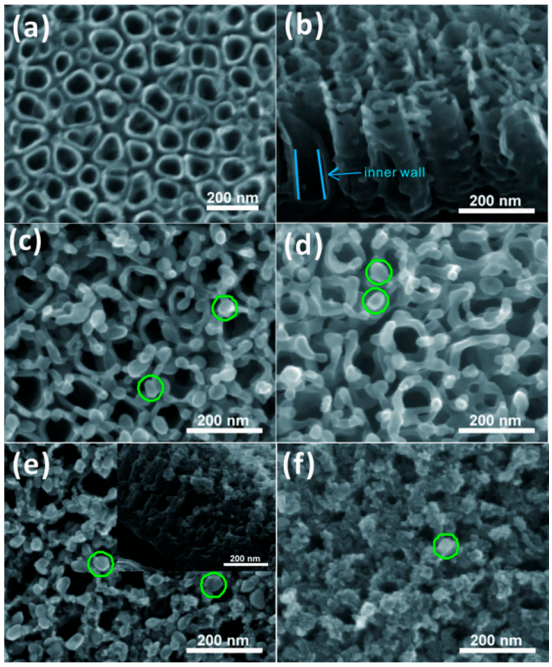

Figure 1. (**a**) Top and (**b**) side view SEM images of TiO_2 nanotube arrays (TNTs). Top view SEM images of $LaFeO_3$ nanoparticle-modified TNTs (LFO/TNTs) prepared by hydrothermal deposition for (**c**) 8 h, (**d**) 10 h, (**e**) 12 h, and (**f**) 14 h (green circles indicate LFO nanoparticles).

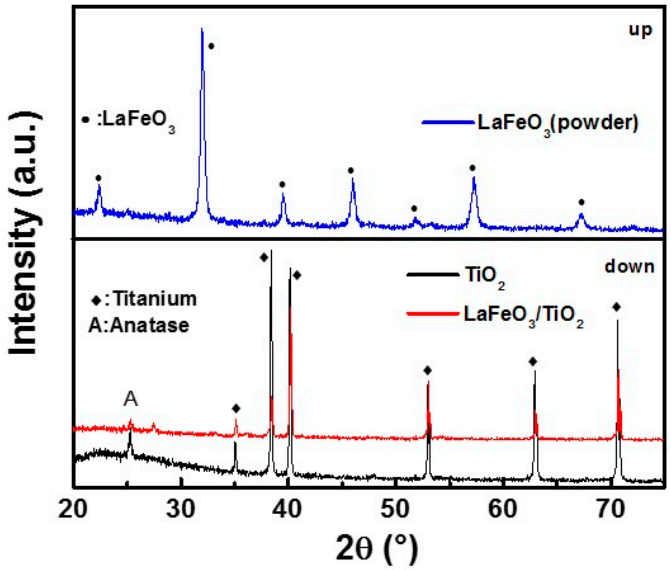

Figure 2. XRD patterns of TNTs, LFO/TNTs, and $LaFeO_3$ powders, respectively.

Further, the chemical states and elemental composition of LFO nanoparticles loaded on the TNTs were studied using XPS. The binding energy values for these components were adjusted by applying C 1*s* 284.4 eV peak as the reference. The ordinary XPS survey spectrum collected from the LFO/TNTs-12h shown in Figure 3a confirms the existence of C 1*s*, Fe 2*p*, La 3*d*, and O 1*s*. The signal of carbon can be attributed to the residual carbon on the surface of the sample. It can be observed from Figure 3c that the peaks located at 724.4 eV and 710.6 eV are attributed to the binding energies of Fe $2p_{1/2}$ and $2p_{3/2}$, respectively [29]. It is notable that shoulder peaks didn't appear in the Fe 2*p* spectra, which means that Fe primarily shows +3 oxidation state. The high resolution spectrum in Figure 3b shows the representative peaks of La $3d_{3/2}$ and La $3d_{5/2}$ emerging at 851.8 and 855.4 eV and at 834.6 and 838.8 eV, respectively. The difference of spin-orbit splitting between La $3d_{5/2}$ and La $3d_{3/2}$ is about 16.8 eV,

which is in accordance with the previous report [30]. The line of the La 3*d* core-level revealed that the La primarily shows a valence state of +3 [29]. The XPS spectra further confirms the prepared nanoparticles to be stoichiometric $LaFeO_3$. The wide and asymmetric O 1*s* XPS spectra in Figure 3d indicates that there are two different chemical states of O, including the anionic oxygen in the TiO_2 lattice (O1*s* (1) dominant peak at 529.9 eV) [31] and the chemisorbed oxygen species (O 1*s* (2) peak at 531.54 eV). The O 1*s* binding energy of the lattice oxygen is generally lower than that of the O^{2-} or OH^- species by 2.1–2.5 eV. Lanthanum oxide is known to be hygroscopic, the corresponding higher O 1*s* peak (531.54 eV) is attributed to the absorbed water molecule. The OH-XPS signal observed for the LFO nanoparticles is associated with the adsorbed water species [32].

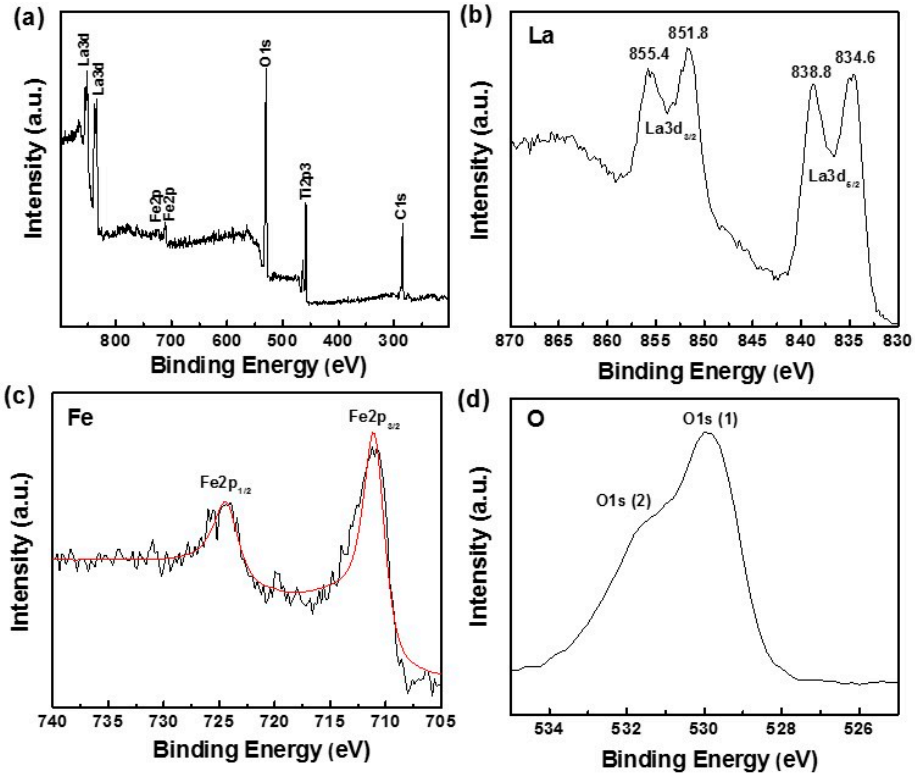

Figure 3. XPS spectra of $LaFeO_3/TiO_2$ nanotube arrays: (**a**) a survey XPS spectrum and high resolution spectra of Fe (**b**), La (**c**), and O (**d**).

The DRS spectra of TNTs, LFO/TNTs-8h, LFO/TNTs-10h, LFO/TNTs-12h, and LFO/TNTs-14h are shown in Figure 4a. For the TNTs, the onset position of light absorption is around 380 nm with a band gap of 3.2 eV. Several satellite peaks can be found in the visible region which is supposed to be caused by the sub-bandgap states of the TNTs [33]. Compared to TNTs, the series of LFO/TNTs exhibits an absorption edge that is obviously red-shifted with a clear absorption of visible light. Another way to make this conclusion is simply by visual observation of these samples, as their color regularly turns from violet to yellowish-green. This means that the light absorption of modified samples is expanded to the visible region of the solar spectrum (up to λ = 550 nm), which is a fundamental condition for the fabrication of visible light-driven photocatalysts. By changing the hydrothermal reaction time (from 8 to 14 h), the absorption edge of each LFO/TNTs changes slightly, with LFO/TNTs-12h exhibiting the widest absorption in the visible region. Figure 4b shows the $(\alpha h\nu)^{1/2}$–$h\nu$ curve derived from the equation $(\alpha h\nu)^2 = k(h\nu - E_g)$, where E_g, ν, h, and α represent the band energy, light frequency, Planck constant, and adsorption coefficient, respectively [34]. It is clear that the band gap of the LFO/TNTs composites decreased sharply from 3.2 to 2.1 eV after the deposition of LFO nanoparticles on the TNTs, thanks to the narrow band gap of LFO (2.1 eV) for sensitizing visible light irradiation.

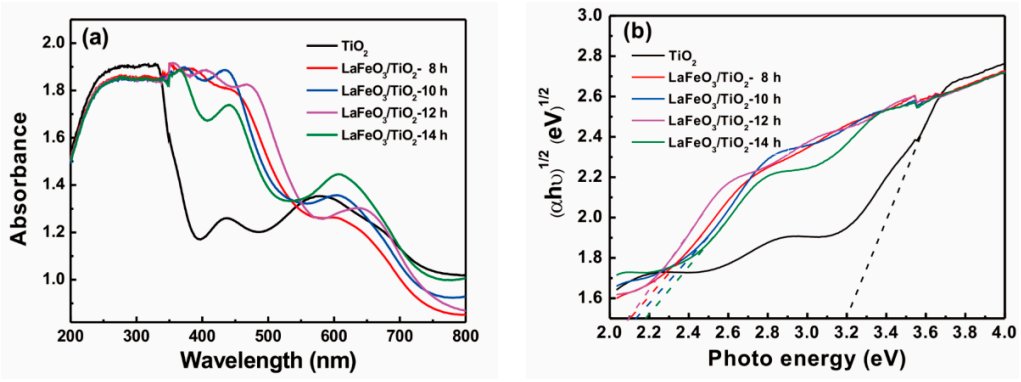

Figure 4. (**a**) DRS spectra and (**b**) $(\alpha hv)^{1/2}$–hv of TiO_2 nanotube arrays and $LaFeO_3/TiO_2$ nanotube arrays with different hydrothermal reaction time.

Photoluminescence (PL) spectroscopy is a powerful tool to study the behavior of charge carrier, such as trapping, immigration, and transfer, as well as to comprehend the processes concerning the recombination of electron–hole pairs [35]. Briefly, upon irradiation, electron–hole pairs experience a recombination process to emit photons and then produce PL [36]. In this work, Figure 5 shows the PL spectra of TNTs and LFO/TNTs composites (excited at 325 nm) in the wavelength range of 400–600 nm. For pristine TNTs, a broad-band emission peak around 450 nm may be related to the recombination of photoexcited electron–hole pairs occupying the singly ionized oxygen vacancies in TiO_2. The shoulder peak observed at around 465 nm is attributed to the oxygen vacancies [37]. Besides, compared to pure TNTs, all LFO/TNTs samples exhibit lower PL intensity, suggesting a higher photocatalytic activity due to the slower recombination rate of electron–hole pairs.

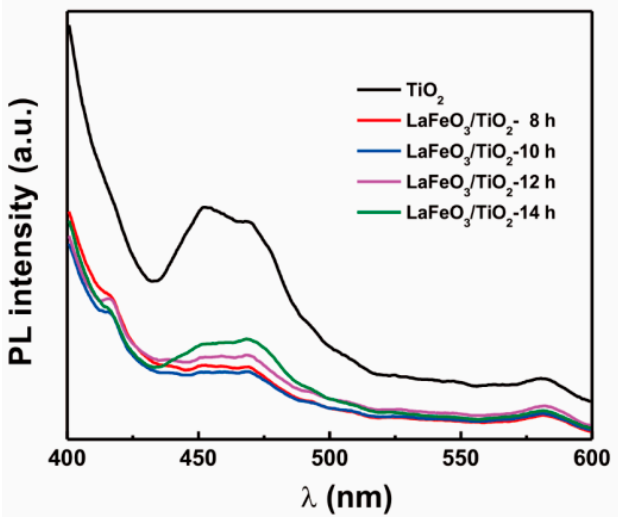

Figure 5. PL spectra of TiO_2 nanotube arrays and $LaFeO_3/TiO_2$ nanotube arrays.

The photocatalytic activities of pure TNTs and LFO/TNTs composites with different hydrothermal reaction times were estimated by observing a photodegradation of the MB aqueous solution (10 mg L^{-1}) under visible light irradiation and the photodegradation kinetics of the MB dye are shown in Figure 6. All samples show a photocatalytic reaction following a pseudo first-order reaction mechanism, which could be simulated as $\ln(C/C_0) = -kt$, where C_0, C, and t are the initial and reaction concentrations and reaction time of the MB aqueous solution, respectively. k is the apparent first-order reaction constant. It can be seen from Figure 6 that pure TNT (0.00073 min^{-1}) showed no better photocatalytic activity than MB self-degradation (0.00068 min^{-1}) under visible light, indicating that TNTs have little effect on accelerating the decomposition rate of MB dye under visible light illumination. Unlike the tiny amount of MB removal by TNTs, in contrast, the degradation efficiency of

the LFO/TNTs samples under the same experiment conditions was much higher, which reveals that LFO/TNTs samples are readily excited under light irradiation, and photogenerated holes accelerate the oxidation of MB dye before recombination with electrons. This result is consistent with our previous work [38]. Obviously, on this occasion, the optimal hydrothermal reaction time is 12 h, and the photocatalytic activity (0.00208 min^{-1}) was triple that of the TNTs. In spite of the LFO/TNTs-14 h sample having a higher amount of LFO than LFO/TNTs-12h, the reason for why LFO/TNTs-12h shows the best photodegradation performance other than LFO/TNTs-14h is that the LFO/TNTs-12h sample can absorb visible light effectively without having the opening of TiO_2 TNTs blocked. Whereas, according to the SEM results, a 14 h reaction time causes excessive accumulation of $LaFeO_3$ nanoparticles, thus blocking the openings of TiO_2 TNTs and leading to the loss of the high surface ratio of the nanotube arrays.

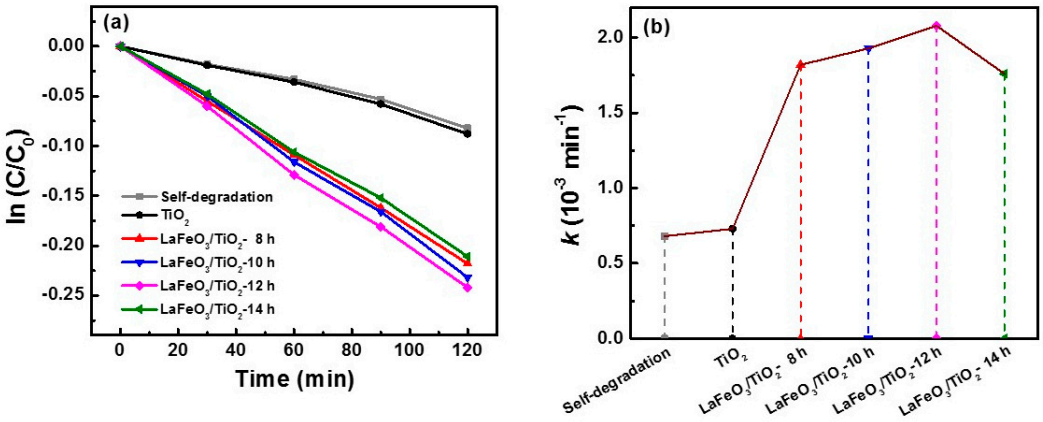

Figure 6. (**a**) Photodegradation rate of MB for TiO_2 nanotube arrays and $LaFeO_3/TiO_2$ nanotube arrays prepared with different hydrothermal reaction times; (**b**) The reaction constant *k* of each sample.

In this paper, the concepts of electronegativity were introduced to estimate the valence band edge position of FLO/TiO_2 heterostructures. Therefore, to calculate the valence band and conduction band edges of FLO/TiO_2 composites at the point of zero charge requires two formulas $E_{VB} = X - E^e + 0.5E_g$ and $E_{CB} = E_{VB} - E_g$. [39–41], where E_g, E^e, and X represent the band gap energy of the semiconductor, the energy of free electrons (about 4.5 eV), and the electronegativity of the semiconductor, respectively, which is the geometric mean of the electronegativity of the integral atoms. The X values for TiO_2 and LFO are calculated to be ca. 5.8 and 5.7 eV, and the E_{VB} of TiO_2 and LFO can be achieved for 2.9 eV and 2.3 eV after substituting X into the equation, respectively. Therefore, the conduction band potentials of TiO_2 and LFO were calculated to be −0.3 eV and 0.2 eV, respectively. Figure 7 shows the band gap structure and possible charge carriers transfer between LFO and TiO_2 under visible light illumination. In general, LFO shows a feature of p-type semiconductor with the corresponding Fermi position near to the valence band [42], while TiO_2 is known as an n-type semiconductor whose Fermi position lies next to the conduction band [43], as shown in Figure 7a. After coupling TiO_2 with LFO to form the p-n heterojunction, the Fermi level of LFO is lifted up, while the Fermi level of TiO_2 is dragged down, until they are at the same level and reach equilibrium (Figure 7b).

Meanwhile, with the increase/decrease of the Fermi position, the complementary energy bands of LFO and TiO_2 move in the opposite directions, i.e., rising for LFO and lowering for TiO_2, resulting in the conduction band position of p-type LFO being higher than that of n-type TiO_2. Thus, the electron–hole pairs have been effectively separated due to this superior energy band structure, resulting in enhanced photocatalytic efficiency under visible-light irradiation. Upon visible light illumination, the electrons of LFO are excited and flow from the valence band (VB) to the conduction band (CB), creating electron–hole pairs. The holes left on the VB of LFO could react with the surface OH^- to yield ·OH, while the excited electrons could effectively transfer to CB of TiO_2 and then

convert dissolved O_2 to $\cdot O_2^-$. Both ·OH and $\cdot O_2^-$ are powerful oxidative species that can efficiently decompose MB dye.

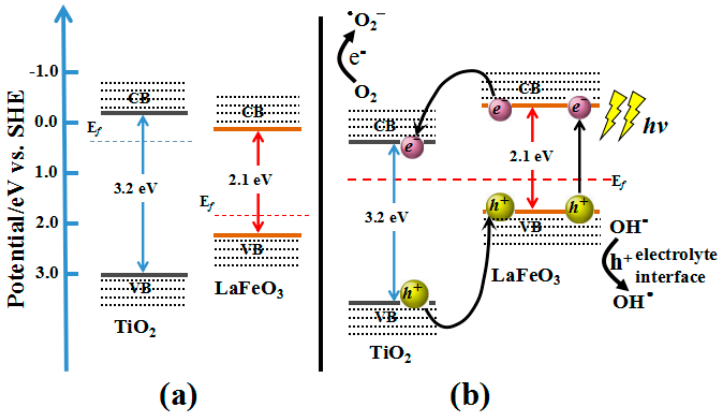

Figure 7. Schematic diagram showing the separation and transfer of charge carriers of p-$LaFeO_3$ and n-TiO_2 under visible light irradiation: (**a**) before and (**b**) after Fermi level reach equilibrium.

4. Conclusions

In summary, a p-n heterojunction LFO/TNTs photocatalyst was synthesized by a facile combination of electrochemical anodization and a hydrothermal method. The as-prepared LFO/TNTs could not only harvest UV light, but could also absorb visible light. The LFO/TNTs composites exhibit high photodegradation thanks to the construction of a p–n heterojunction between LFO and TiO_2 which can efficiently constrain the recombination of electron–hole pairs and facilitate rapid photoexcited electron transfer from p-type LFO to n-type TNTs. Besides, the advantages of easy separation from the polluted solution without second contamination and re-usability make the prepared LFO/TNTs an excellent photocatalyst for commercial applications. Besides LFO, this general strategy can also provide an effective tool for fabricating other ABO_3 perovskite semiconductor nanoparticle-modified TiO_2 nanotube array composites which exhibit promising prospects in other areas, such as water splitting and energy storage, etc.

Author Contributions: Conceptualization, Y.T., L.S. and Y.L.; Data Curation, J.Y. and Z.Z.; Formal Analysis, S.X., J.H., Y.T., C.L. and Y.L.; Investigation, J.Y.; Methodology, J.Y. and M.G.; Project Administration, J.Y. and L.S.; Supervision, L.S. and C.L.; Validation, Z.Z.; Writing–Original Draft, J.Y.; Writing–Review & Editing, S.X., M.G., J.H., Y.T., L.S., C.L. and Y.L.

Funding: This research was funded by National Natural Science Foundation of China (Nos. 21621091 and 21501127) and Guangdong Natural Science Foundation (No. 2016A030313845).

Conflicts of Interest: The authors declare no conflict of interest.

References

1. Wang, M.; Iocozzia, J.; Sun, L.; Lin, C.; Lin, Z. Inorganic-modified semiconductor TiO_2 nanotube arrays for photocatalysis. *Energy Environ. Sci.* **2014**, *7*, 2182–2202. [CrossRef]
2. Tang, Y.; Jiang, Z.; Xing, G.; Li, A.; Kanhere, P.D.; Zhang, Y.; Sum, T.C.; Li, S.; Chen, X.; Dong, Z.; et al. Efficient Ag@AgCl cubic cages photocatalyst profited from ultrafast plasmon-induced electron transfer process. *Adv. Funct. Mater.* **2013**, *23*, 2932. [CrossRef]
3. Tang, Y.; Zhang, Y.; Malyi, O.I.; Bucher, N.; Xia, H.; Xi, S.; Zhu, Z.; Lv, Z.; Li, W.; Wei, J.; et al. Identifying the origin and contribution of surface storage in TiO_2(B) nanotube electrode by in-situ dynamic valence state monitoring. *Adv. Mater.* **2018**, *30*, 1802200. [CrossRef] [PubMed]
4. Riboni, F.; Nguyen, N.T.; So, S.; Schmuki, P. Aligned metal oxide nanotube arrays: Key-aspects of anodic TiO_2 nanotube formation and properties. *Nanoscale Horizons* **2016**, *1*, 445–466. [CrossRef]

5. Ge, M.-Z.; Cao, C.-Y.; Li, S.-H.; Tang, Y.-X.; Wang, L.-N.; Qi, N.; Huang, J.-Y.; Zhang, K.-Q.; Al-Deyab, S.S.; Lai, Y.K. In situ plasmonic Ag nanoparticle anchored TiO_2 nanotube arrays as visible-light-driven photocatalysts for enhanced water splitting. *Nanoscale* **2016**, *8*, 5226–5234. [CrossRef] [PubMed]
6. Cai, J.; Shen, J.; Zhang, X.; Ng, Y.H.; Huang, J.; Guo, W.; Lin, C.; Lai, Y. Light-driven sustainable hydrogen production utilizing TiO_2 nanostructures: A review. *Small Methods* **2018**, *2*, 1800184. [CrossRef]
7. Ye, M.; Gong, J.; Lai, Y.; Lin, C.; Lin, Z. High-efficiency photoelectrocatalytic hydrogen generation enabled by palladium quantum dots-sensitized TiO_2 nanotube arrays. *J. Am. Chem. Soc.* **2012**, *134*, 15720–15723. [CrossRef] [PubMed]
8. Macak, J.M.; Zlamal, M.; Krysa, J.; Schmuki, P. Self-organized TiO_2 nanotube layers as highly efficient photocatalysts. *Small* **2007**, *3*, 300–304. [CrossRef] [PubMed]
9. Zhang, G.; Huang, H.; Zhang, Y.; Chan, H.L.; Zhou, L. Highly ordered nanoporous TiO_2 and its photocatalytic properties. *Electrochem. Commun.* **2007**, *9*, 2854–2858. [CrossRef]
10. Ge, M.; Cao, C.; Huang, J.; Li, S.; Chen, Z.; Zhang, K.-Q.; Al-Deyab, S.S.; Lai, Y. A review of one-dimensional TiO_2 nanostructured materials for environmental and energy applications. *J. Mater. Chem. A* **2016**, *4*, 6772–6801. [CrossRef]
11. Ge, M.; Li, Q.; Cao, C.; Huang, J.; Li, S.; Zhang, S.; Chen, Z.; Zhang, K.; Al-Deyab, S.S.; Lai, Y. One-dimensional TiO_2 nanotube photocatalysts for solar water splitting. *Adv. Sci.* **2017**, *4*, 1600152. [CrossRef] [PubMed]
12. Kowalski, D.; Kim, D.; Schmuki, P. TiO_2 nanotubes, nanochannels and mesosponge: Self-organized formation and applications. *Nano Today* **2013**, *8*, 235–264. [CrossRef]
13. Lai, Y.; Huang, J.; Zhang, H.; Subramaniam, V.-P.; Tang, Y.-X.; Gong, D.-G.; Sundarb, L.; Sun, L.; Chen, Z.; Lin, C.J. Nitrogen-doped TiO_2 nanotube array films with enhanced photocatalytic activity under various light sources. *J. Hazard. Mater.* **2010**, *184*, 855–863. [CrossRef] [PubMed]
14. Ge, M.Z.; Cai, J.S.; Iocozzia, J.; Cao, C.; Huang, J.; Zhang, X.; Shen, J.; Wang, S.; Zhang, S.; Zhang, K.-Q.; et al. A review of TiO_2 nanostructured catalysts for sustainable H_2 generation. *Int. J. Hydrog. Energy* **2017**, *42*, 8418–8449. [CrossRef]
15. Li, H.; Zhou, Y.; Tu, W.; Ye, J.; Zou, Z. State-of-the-art progress in diverse heterostructured photocatalysts toward promoting photocatalytic performance. *Adv. Funct. Mater.* **2015**, *25*, 998–1013. [CrossRef]
16. Jia, L.; Li, J.; Fang, W. Enhanced visible-light active C and Fe co-doped $LaCoO_3$ for reduction of carbon dioxide. *Catal. Commun.* **2009**, *11*, 87–90. [CrossRef]
17. Wheeler, G.P.; Choi, K.-S. photoelectrochemical properties and stability of nanoporous p-Type $LaFeO_3$ photoelectrodes prepared by electrodeposition. *ACS Energy Lett.* **2017**, *2*, 2378–2382. [CrossRef]
18. Dhinesh Kumar, R.; Thangappan, R.; Jayavel, R. Enhanced visible light photocatalytic activity of $LaMnO_3$ nanostructures for water purification. *Res. Chem. Intermed.* **2018**, *44*, 4323–4337. [CrossRef]
19. Truppi, A.; Petronella, F.; Placido, T.; Striccoli, M.; Agostiano, A.; Curri, M.L.; Comparelli, R. Visible-light-active TiO_2-based hybrid nanocatalysts for environmental applications. *Catalysts* **2017**, *7*, 100. [CrossRef]
20. Farhadi, S.; Amini, M.M.; Mahmoudi, F. Phosphotungstic acid supported on aminosilica functionalized perovskite-type $LaFeO_3$ nanoparticles: A novel recyclable and excellent visible-light photocatalyst. *RSC Adv.* **2016**, *6*, 102984–102996. [CrossRef]
21. Guo, M.; Xie, K.; Lin, J.; Yong, Z.; Zhou, L.; Wang, Y.; Huang, H. Design and coupling of multifunctional TiO_2 nanotube photonic crystal to nanocrystalline titania layer as semi-transparent photoanode for dye-sensitized solar cell. *Energy Environ. Sci.* **2012**, *5*, 9881–9888. [CrossRef]
22. Nguyen, N.T.; Altomare, M.; Yoo, J.E.; Taccardi, N.; Schmuki, P. Noble metals on anodic TiO_2 nanotube mouths: Thermal dewetting of minimal Pt Co-catalyst loading leads to significantly enhanced photocatalytic H_2 generation. *Adv. Energy Mater.* **2016**, *6*, 1501926. [CrossRef]
23. Xie, K.; Sun, L.; Wang, C.; Lai, Y.; Wang, M.; Chen, H.; Lin, C. Photoelectrocatalytic properties of Ag nanoparticles loaded TiO_2 nanotube arrays prepared by pulse current deposition. *Electrochim. Acta* **2010**, *55*, 7211–7218. [CrossRef]
24. Zhou, K.; Wu, X.; Wu, W.; Xie, J.; Tang, S.; Liao, S. Nanocrystalline $LaFeO_3$ preparation and thermal process of precursor. *Adv. Powder Technol.* **2013**, *24*, 359–363.
25. Parida, K.M.; Reddy, K.H.; Martha, S.; Das, D.P.; Biswal, N. Fabrication of nanocrystalline $LaFeO_3$: An efficient sol-gel auto-combustion assisted visible light responsive photocatalyst for water decomposition. *Int. J. Hydrogen Energy* **2010**, *35*, 12161–12168. [CrossRef]

26. Wang, Y.; Zhu, J.; Zhang, L.; Yang, X.; Lu, L.; Wang, X. Preparation and characterization of perovskite $LaFeO_3$ nanocrystals. *Mater. Lett.* **2006**, *60*, 1767–1770. [CrossRef]
27. Yu, J.; Wang, B. Effect of calcination temperature on morphology and photoelectrochemical properties of anodized titanium dioxide nanotube arrays. *Appl. Catal. B* **2010**, *94*, 295–302. [CrossRef]
28. Phoon, B.L.; Lai, C.W.; Pan, G.T.; Yang, T.C.K.; Juan, J.C. One-pot hydrothermal synthesis of strontium titanate nanoparticles photoelectrode using electrophoretic deposition for enhancing photoelectrochemical water splitting. *Ceram. Int.* **2018**, *44*, 9923–9933. [CrossRef]
29. Flynn, B.T.; Zhang, L.; Shutthanandan, V.; Varga, T.; Colby, R.J.; Oleksak, R.P.; Manandhar, S.; Engelhard, M.H.; Chambers, S.A.; Henderson, M.A.; et al. Growth and surface modification of $LaFeO_3$ thin films induced by reductive annealing. *Appl. Surf. Sci.* **2015**, *330*, 309–315. [CrossRef]
30. Zhang, C.; Wang, C.; Zhan, W.; Guo, Y.; Guo, Y.; Lu, G.; Baylet, A.; Giroir-Fendler, A. Catalytic oxidation of vinyl chloride emission over $LaMnO_3$ and $LaB_{0.2}Mn_{0.8}O_3$ (B = Co, Ni, Fe) catalysts. *Appl. Catal. B* **2013**, *129*, 509–516. [CrossRef]
31. Simmons, G.W.; Beard, B.C. Characterization of acid-base properties of the hydrated oxides on iron and titanium metal surfaces. *J. Phys. Chem.* **1987**, *91*, 1143–1148. [CrossRef]
32. Thirumalairajan, S.; Girija, K.; Hebalkar, N.Y.; Mangalaraj, D.; Viswanathan, C.; Ponpandian, N. Shape evolution of perovskite $LaFeO_3$ nanostructures: A systematic investigation of growth mechanism, properties and morphology dependent photocatalytic activities. *RSC Adv.* **2013**, *3*, 7549–7561. [CrossRef]
33. Lai, Y.; Sun, L.; Chen, Y.; Zhuang, H.; Lin, C.; Chin, J.W. Effects of the structure of TiO_2 nanotube array on Ti substrate on its photocatalytic activity. *J. Electrochem. Soc.* **2006**, *153*, D123–D127. [CrossRef]
34. Vijayan, B.K.; Dimitrijevic, N.M.; Wu, J.; Gray, K.A. The effects of Pt doping on the structure and visible light photoactivity of titania nanotubes. *J. Phys. Chem. C* **2010**, *114*, 21262–21269. [CrossRef]
35. Yamashita, H.; Harada, M.; Misaka, J.; Takeuchi, M.; Neppolian, B.; Anpo, M. Photocatalytic degradation of organic compounds diluted in water using visible light-responsive metal ion-implanted TiO_2 catalysts: Fe ion-implanted TiO_2. *Catal. Today* **2003**, *84*, 191–196. [CrossRef]
36. Zhang, N.; Liu, S.; Fu, X.; Xu, Y.J. Synthesis of M@TiO_2 (M = Au, Pd, Pt) core-shell nanocomposites with tunable photoreactivity. *J. Phys. Chem. C* **2011**, *115*, 9136–9145. [CrossRef]
37. Lei, Y.; Zhang, L.D.; Meng, G.W.; Li, G.H.; Zhang, X.Y.; Liang, C.H.; Zhang, X.Y.; Liang, C.H.; Chen, W.; Wang, S.X. Preparation and photoluminescence of highly ordered TiO_2 nanowire arrays. *Appl. Phys. Lett.* **2001**, *78*, 1125–1127. [CrossRef]
38. Xiang, S.; Zhang, Z.; Gong, C.; Wu, Z.; Sun, L.; Ye, C.; Lin, C. $LaFeO_3$ nanoparticle-coupled TiO_2 nanotube array composite with enhanced visible light photocatalytic activity. *Mater. Lett.* **2018**, *216*, 1–4. [CrossRef]
39. Zhang, X.; Zhang, L.; Xie, T.; Wang, D. Low-temperature synthesis and high visible-light-induced photocatalytic activity of BiOI/TiO_2 heterostructures. *J. Phys. Chem. C* **2009**, *113*, 7371–7378. [CrossRef]
40. Lin, X.; Xing, J.; Wang, W.; Shan, Z.; Xu, F.; Huang, F. Photocatalytic activities of heterojunction semiconductors Bi_2O_3/$BaTiO_3$: A strategy for the design of efficient combined photocatalysts. *J. Phys. Chem. C* **2007**, *111*, 18288–18293. [CrossRef]
41. Butler, M.A.; Ginley, D.S. Prediction of flatband potentials at semiconductor-electrolyte interfaces from atomic electronegativities. *J. Electrochem. Soc.* **1978**, *125*, 228–232. [CrossRef]
42. Fan, H.; Zhang, T.; Xu, X.; Lv, N. Fabrication of N-type Fe_2O_3 and P-type $LaFeO_3$ nanobelts by electrospinning and determination of gas-sensing properties. *Sens. Actuators B Chem.* **2011**, *153*, 83–88. [CrossRef]
43. Khan, M.; Al-Shahry, M.; Ingler, W.B. Efficient photochemical water splitting by a chemically modified n-TiO_2. *Science* **2002**, *297*, 2243–2245. [CrossRef] [PubMed]